doi:10.1016/j.jmb.2006.11.032 J. Mol. Biol. (2007) 371, 787–799

JMB

Available online at www.sciencedirect.com

ScienceDirect

ELSEVIER

The Crystal Structure of the Dps2 from *Deinococcus radiodurans* Reveals an Unusual Pore Profile with a Non-specific Metal Binding Site

M.G. Cuypers[1], E.P. Mitchell[1], C.V. Romão[2] and S.M. McSweeney[1]*

[1]*ESRF (European Synchrotron Radiation Facility) 6 rue Jules Horowitz, BP 220 38043 Grenoble, France*

[2]*Instituto de Tecnologia Química e Biológica Av. da República (EAN) 2784 - 505 Oeiras, Portugal*

**Corresponding author*

The crystal structure of recombinant Dps2 (DRB0092, DNA protecting protein under starved conditions) from the Gram-positive, radiation-resistant bacterium *Deinococcus radiodurans* has been determined in its apo and iron loaded states. Like other members of the Dps family, the bacterial *Dr*Dps2 assembles as a spherical dodecamer with an outer shell diameter of 90 Å and an interior diameter of 40 Å. A total of five iron sites were located in the iron loaded structure, representing the first stages of iron biomineralisation. Each subunit contains a mononuclear iron ferroxidase centre coordinated by residues highly conserved amongst the Dps family of proteins. In the structures presented, a distinct iron site is observed 6.1 Å from the ferroxidase centre with a unique ligand configuration of mono coordination by the protein and no bridging ligand to the ferroxidase centre. A non-specific metallic binding site, suspected to play a regulative role in iron uptake/release from the cage, was found in a pocket located near to the external edge of the C-terminal 3-fold channel.

Keywords: Dps; *Deinococcus radiodurans*; ferroxidase centre; iron nucleation; iron channels

Introduction

The Dps (DNA protecting protein under starved conditions) family of microbial proteins is widely spread in bacteria and archaea.[1–13] Dps proteins are considered to be functionally close to ferritins but differ structurally with a dodecamer assembly compared to ferritins, which form 24-meric structures.[14–16] Members of the Dps family possess many different, but related, functions including oxidative stress protection, DNA protection by physical shielding and iron uptake and storage.[17,18] The characteristic spherical structure of Dps is composed of 12 identical four helix bundle monomers with 23 symmetry.[3,19] The hollow shell formed has a typical external diameter of between 80 to 90 Å and an internal diameter of 40 to 50 Å.[3,17,19–22] Dps proteins have an iron binding capacity of around 400 to 500 iron atoms per protein spherical assembly[23,24] compared to a maximum of 4500 for typical ferritins.[14]

The Dps family members show ferroxidase activity *via* a mononuclear active site which is shared by two subunits related by a 2-fold rotational symmetry axis.[5–7,10,17,19,22,24,25] The ferroxidase site is the key that confers fast iron oxidation capability to Dps, in turn preventing the formation of highly cytotoxic reactive oxygen species (ROS) from the reaction of iron (II) with hydrogen peroxide or dioxygen.[6,18,19,21,26] Iron is then stored and maintained in a safe, non-toxic form unavailable for Fenton chemistry.[27] The exposure of *Deinococcus radiodurans* to a dose of 10 kGy of ionising radiation results in about 100 double strand breaks per chromosome, which are repaired without lethality, mutagenesis or rearrangement, whereas other organisms cannot survive such a dose.[28,29] The DNA damage resistance of *D. radiodurans* may be due to highly efficient DNA repair.[29,30] It is likely that additional cellular measures play an important role in cell survival. It has been proposed that the genome of *D. radiodurans* harbours two Dps encoding genes: *Dr*Dps1 is the product of DR2263 and *Dr*Dps2 the product of DRB0092.[29,31,32] The protein sequences have only 14 % identity. Two distinct Dps genes encoded in the same organism are observed in *D. radiodurans*[29,31,32] and *Bacillus anthracis*[10] but also in

E-mail address of the corresponding author: seanmcs@esrf.fr

0022-2836/$ - see front matter © 2007 Published by Elsevier Ltd.

other species of *Baccillus*.[33,34] The difference in the cellular role of the two Dps in the bacteria remains unknown.[31] In the case of *D. radiodurans*, an analysis of the transcriptome dynamics[35] and the temporal profile for expression levels of both proteins did not clarify the roles of either protein.

The ubiquitous starvation-induced DNA-binding protein Dps is thought to play a protective role towards DNA. Dps may associate with DNA into a non-specific Dps-DNA complex to minimise DNA cleavage caused by reactive oxygen species, as well as sequestering iron ions and making DNA inaccessible to degradation enzymes.[6,18,19,21,26] Helices of variable length and rich in positively charged lysine or arginine residues, which protrude from the external surface of the Dps spherical assembly, are thought to stabilise the complex with DNA.[18,23,32,36] Such extensions are observed on the C-terminal of *Mycobacterium smegmatis* Dps[9,22] and on the N-terminal of *Escherichia coli* Dps,[12] *Lactococcus lactis*[36] Dps and *Bacillus subtilis* MrgA.[13] The absence of these extensions correlates with the lack of DNA binding observed in *Listeria innocua* Dps,[4,20,37] the related *B. anthracis*[10] Dlp-1 and Dlp-2 and *Helicobacter pylori* neutrophil-activating protein (HP-NAP).[38] It has also been reported that for *Agrobacterium tumefaciens* Dps[19] the lack of freedom and flexibility of the lysine-rich N-terminal extension could be the reason for absence of DNA binding. In general for the Dps proteins, *in vitro* DNA protection against oxidative stress is not only dependent on the formation of a protein-DNA complex but also on the conservation of a functional ferroxidase centre.[19]

The extremely high resistance of the bacterium *D. radiodurans* to damage by ionising radiation and the presence of two Dps proteins, able to help minimise free radical production and possibly protect DNA, in its genome led us to determine the crystal structure of *Dr*Dps2 (gene DRB0092) in its apo state and in states indicative of the first stages of iron loading. These structures are compared to the known structures of Dps from other organisms.

Results

The detailed structure of a truncated form of *Dr*Dps2 without the first 30 N-terminal residues is presented here.

Model quality and completeness

The crystal structure contains one subunit per asymmetric unit, which is a property shared so far by *Mycobacterium smegmatis* Dps[9] and *D. radiodurans* *Dr*Dps1.[31,39] The Matthews coefficient for the model is 2.84 A^3/Da, suggesting a solvent content for the refined apo and iron soaked models of 56 %. Ramachandran plots[40] of both structures show that 93.9% and 93.2%, respectively, of residues are located in the most favoured regions and, in both cases, with no residues in the disallowed region.

The electron density maps of the 2.05 Å resolution apo and the 2.10 Å resolution iron soaked forms show weak or absence of electron density for the 41 N-terminal and five C-terminal residues out of 211 residues for the cloned protein (see Materials and Methods). Mass spectrometry analysis confirmed the presence of 211 residues in the fresh pure sample. However, mass spectrometry analysis of a sample of solubilised crystals showed a mixture of lower molecular masses than expected, suggesting protein degradation in the crystals (corresponding to a maximum of 32 residues missing). The N-terminal peptide residues missing in the model are likely to be located (by extrapolation from the first detected residue on the N-terminal side) on the external face of the protein dodecamer and in the bulk solvent surrounding the protein. The absence of electron density for the extremities of the protein chain is not unique amongst the Dps family.[12] Commencing at residue 42, the electron density of both apo and iron soaked models can be traced throughout the main chain without interruption. However, regions of weaker electron density occur from residue Thr42 to Lys47 and Ala120 to Glu125 corresponding to disordered areas with higher mobility and higher atomic *B*-factors. The superposition of the C-alpha atoms of the apo and iron soaked models yields a RMS deviation of 0.343 Å showing that both structures are globally very similar. The statistics for data collection, phasing and refinement are presented in Table 1.

Overall structure of *Dr*Dps2

The monomer of *Dr*Dps2 is composed of a four helix bundle (helices A, B, C and D) with a fifth helix (helix BC) of seven residues oriented almost perpendicular to the bundle and an additional single turn helix (E) at the C terminal formed by residues 197 to 201 (Figure 1(a) and (b)). Short loops connect the helices except for helix BC, which is roughly centred on a long strap-like loop connected to either side to helices B and C. Helices A, B, BC, C and D are composed of residues 42–72, 77–106, 113–120, 133–159 and 162–188, respectively (identically equal to 72–102, 107–136, 143–150, 163–189 and 192–218 from the genomic sequence).

Symmetry-related subunits of *Dr*Dps2, positioned according to the *P*23 crystallographic symmetry operators, yield a globular dodecamer with an average external diameter of ca 90 Å and an internal average diameter of ca 37 Å. The dodecameric assembly forms a cavity with a global volume calculated by VOIDOO[41] of 44,580(±1350) A^3. The internal surface of the shell is lined by residues from helices B and D only. The external surface is made of the helices A, C and BC. The crystallographic symmetry generates two types of 3-fold related channels, the C-terminal and N-terminal pores, which lead into the central cavity of the protein assembly and are described further below. The spherical assembly of *Dr*Dps2 as viewed from the C-terminal 3-fold symmetry axis is represented in

Table 1. Data collection, phasing and refinement statistics

		Apo	Iron soak (20 min 0.1 M $(NH_4)_2Fe(SO_4)_2$)			
	Crystal	A	B	C	C	C
	ESRF Beamline	ID14-2	ID23-1	ID23-1	ID23-1	ID23-1
Data	Space group	*P* 2 3	*P* 2 3	*P* 2 3	*P* 2 3	*P* 2 3
	Wavelength (Å)	0.933	1.7399	1.1070	1.7377	1.7451
	Unit cell dimension (Å)	88.5	88.6	89.0	89.0	89.0
	Resolution (Å)	44.2–2.05	62.4–2.8	29.7–2.1	36.3–2.3	36.3–2.3
	R_{merge}	0.067 (0.501)	0.128 (0.643)	0.089 (0.489)	0.108 (0.518)	0.101 (0.428)
	$R_{r.i.m.}$ (or R_{meas})	0.070 (0.526)	0.139 (0.659)	0.103 (0.571)	0.128 (0.601)	0.116 (0.497)
	$R_{p.i.m.}$	0.015 (0.121)	0.022 (0.102)	0.038 (0.207)	0.048 (0.224)	0.043 (0.186)
	Mean $I/\sigma(I)$	40.4 (5.6)	36.2 (6.5)	16.9 (3.0)	13.9 (2.7)	14.8 (3.3)
	Wilson *B*-factor (Å^2)	29.8	53.2	35.2	42.2	39.3
	Completeness (%)	100.0 (100.0)	100.0 (100.0)	99.9 (100.0)	100.0 (100.0)	100.0 (100.0)
	Multiplicity	21.8 (18.6)	40.8 (40.8)	7.3 (7.4)	7.1 (7.1)	7.1 (7.0)
	Number observations	312,296 (20,355)	239,321 (17,269)	102,174 (7485)	76,686 (5576)	76,320 (5494)
	Number unique reflections	14,773 (1092)	5870 (423)	13,986 (1015)	10,750 (789)	10,737 (783)
Phasing	R_{cullis} (acen.)	–	0.608	–	–	–
	Phasing power (acen.)	–	1.93	–	–	–
	Figure of merit (before solvent flattening)	–	0.467	–	–	–
Refinement	R_{factor}	0.178	–	0.188	–	–
	R_{free}	0.219	–	0.235	–	–
	RMS deviation: bonds (Å)	0.018	–	0.016	–	–
	RMS deviation: angles (°)	1.383	–	1.422	–	–
	Overall *G*-factor	0.17	–	0.13	–	–
	PDB ID	2C2J	–	2C6R	–	–
	Model residues	165	–	166	–	–
	Waters	128	–	135	–	–
	Occupied iron sites	1	–	5	–	–
	Other	Mg^{2+}	–	Cl^-	–	–

Values in parentheses are for the highest resolution shell.

$R_{merge} = \sum |I - \langle I \rangle| / \sum(I)$, where I is the intensity measured for a given reflection, $\langle I \rangle$ is the average intensity for multiple measurements of this reflection.

$R_{r.i.m.} = (\sum [N/(N-1)]^{1/2} \sum |I - \langle I \rangle|) / \sum(I)$, where N is the redundancy.[58]

$R_{p.i.m.} = (\sum [1/(N-1)]^{1/2} \sum |I - \langle I \rangle|) / \sum(I)$.[58]

$R_{cullis} = \sum ||| F_{PH}| \pm |F_P|| - |F_H|| / \sum || F_{PH}| \pm |F_P||$, where F_{PH}, F_P and F_H are the derivative, native and calculated heavy-atom structure factor amplitudes, respectively, for acentric reflections.

Phasing power = r.m.s. of $(|F_H| / E)$, where E is the residual lack of closure error; for acentric reflections.

$R_{factor} = \sum || F_{obs}| - |F_{calc}|| / \sum |F_{obs}|$, where F_{obs} and F_{calc} are the observed and calculated structure factor amplitudes, respectively, for 95% of the reflection data used in refinement.

$R_{free} = \sum || F_{obs}| - |F_{calc}|| / \sum |F_{obs}|$, for 5% of the reflection data excluded during the refinement. The value quoted is for the penultimate refinement cycle (all reflections being used for the final round).

Figure 1(c). The abundance of negatively charged residues on the inner surface of the Dps shell makes the protein compatible with iron bio-mineral entrapment. Preliminary aerobic ferroxidase assays followed by UV-visible spectroscopy (data not shown) support the role of active redox chemistry performed by the protein.

The intensities observed in phased anomalous difference maps (Materials and Methods) at the locations of the irons found in the iron loaded structure and labelled sites 1 to 5 are described in Table 2 for data collected just above and below the iron K absorption edge. Iron sites Fe1, Fe2 and Fe3 have the highest peaks in the phased anomalous difference maps. In the data from the iron soaked crystal, site Fe3 retains a significant peak in the phased anomalous difference map calculated using data collected from below the iron edge, though still showing a change in peak height from above and below the edge, suggesting that this site may be shared between (low occupancy) iron and other unidentified element(s) as discussed later. The anomalous difference peaks from the iron loaded data are weaker for Fe4 and Fe5. The phased anomalous difference maps calculated using the apo data reveal the presence of an iron ion in position Fe4 and a non-iron metal bound in the same site as Fe3, the other metallic sites being unoccupied in the apo crystal structure. The relative intensity of the sulphur peaks of Met183, from both above and below the iron edge, in the phased anomalous difference maps of the apo and the iron loaded structures are similar (data not shown), thereby giving a base line for anomalous peaks between the paired data sets and suggesting that radiation damage effects are not responsible for the changes observed. The iron binding sites located in the structures of the apo and iron loaded Dps and their distances from the site ligands are reported in Table 2 and shown in Figure 1(a). The iron sites themselves are described in detail below.

The ferroxidase centre

The proposed ferroxidase centre, Fe1, is located between two antiparallel Dps subunits and is near to

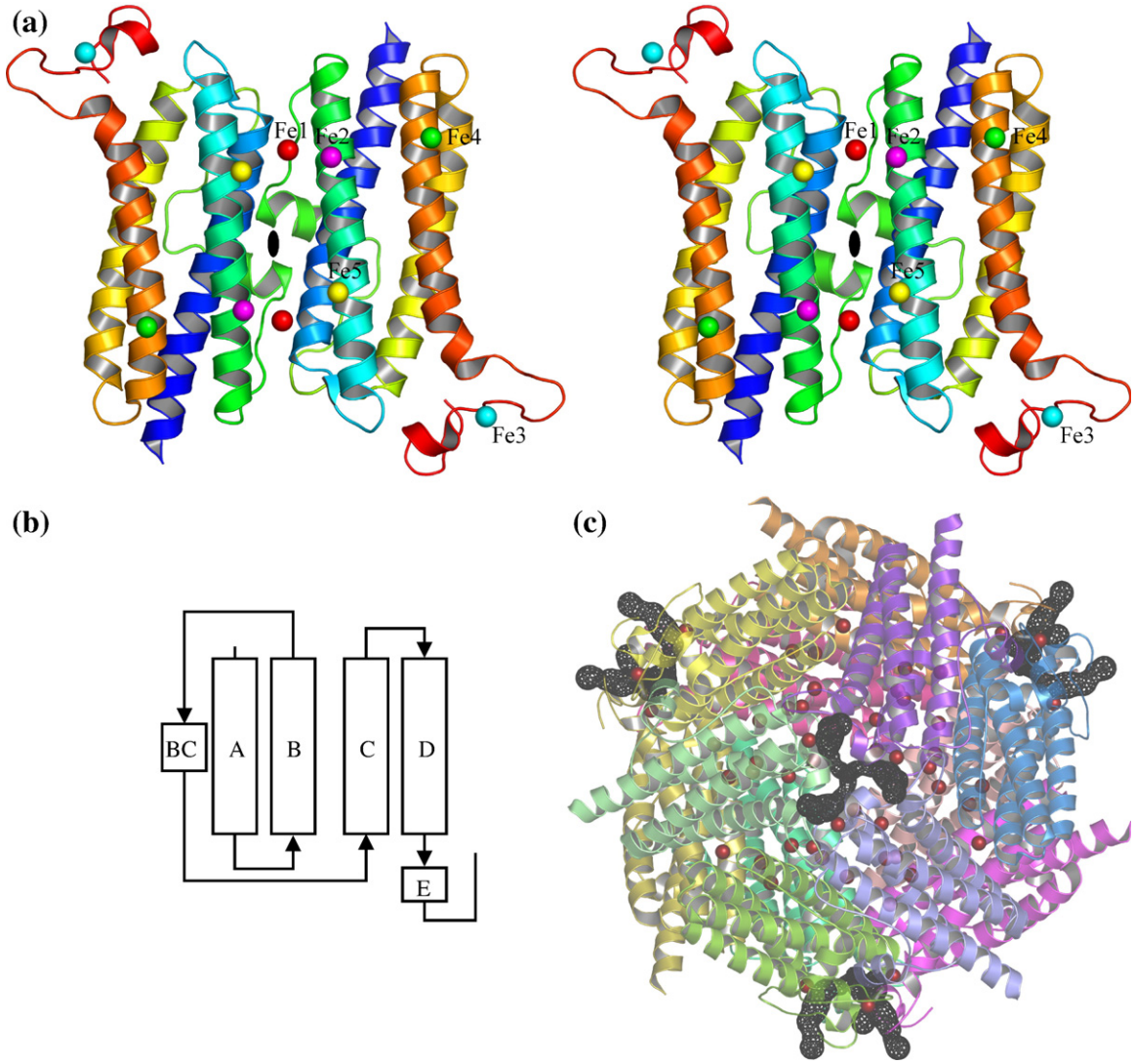

Figure 1. Representation of *Dr*Dps2. (a) Stereo view of the dimeric assembly as seen from the 2-fold axis and inside the sphere. Irons are spheres shown in different colours and labelled: Fe1, red; Fe2, pink; Fe3, cyan; Fe4, green; and Fe5, yellow. The main chain is coloured from blue at the N-terminal to red at the C-terminal. (b) *Dr*Dps2 monomer topology showing helices organisation. (c) The spherical dodecameric assembly viewed from the 3-fold C-terminal channel (black isomesh). Each monomer is in a different colour. Figures prepared with PyMOL [www.pymol.org].

the 2-fold rotation axis resulting in a distance between the two symmetry-related ferroxidase sites of 21 Å. This is a recurrent inter-ferroxidase site distance amongst the Dps family.[17] The ferroxidase site of the apo crystal structure was observed to be metal free. The direct ligands of Fe1 are provided from two different subunits: His70 from one subunit and Asp97 and Glu101 from the other. A water molecule in the octahedral coordination sphere of Fe1 is stabilised through a hydrogen bond with His82 and the water is also ligated with a chloride ion at 3.35 Å distance (Figure 2). A strong peak in the electron density map at 5.21 Å and 4.88 Å from Fe1 and Fe2, respectively, was assigned to the chloride ion, which was possibly introduced during the purification process or, move likely, from the crystallisation solution rather than having a role *in vivo*. This chloride is stabilised by Lys178 at 2.85 Å (Figure 2).

The comparison of the apo-form with the iron soaked structures, by superposition of the C-alphas from only helix B, which contains the relevant residues for the ferroxidase centre, shows a shift in the positions of key residues Asp97 and Glu101 involved in the chelation of Fe1. Their carbonyl side-chains are shifted by ca 1.7 Å and ca 3.7 Å, respectively between both compared structures. Also depending on the presence of iron in the ferroxidase centre, residue Trp71 switches ca 180-degrees between two rotamer conformations. The position of the carboxylic group of Glu101 and Fe1 in the iron soaked model in fact superimposes with the position of the aromatic side-chain of Trp71 in the apo-form model. Once the hydrophobic side-chain of residue Trp71 has flipped out of the ferroxidase site, the acidic chains from Asp97 and Glu101 can chelate iron. In the apo-form structure, the orientation of residue Asp97 is stabilised by a salt-bridge with

Table 2. Observed metal sites and their ligands in the iron soaked and apo *Dr*Dps2 protein

Metal no.	Occupancy	B_{factor} (Å^2)	σ max[a]	Location	Ligand	$d_{Fe\text{-}L}$ (Å)
Fe1 (n/a)	1	32	22.7/4.0 (n/a)	Inside, close to Fe2 (6.12 Å)	Asp97 [$O^{\delta1}$; $O^{\delta2}$]	2.38; 2.37
					Glu101 [$O^{\varepsilon1}$; $O^{\varepsilon2}$]	2.09; 3.36
					His 70 [$N^{\varepsilon1}$]	2.22
					2× O [H_2O]	2.25; 2.29
Fe2 (n/a)	1	52	14.7/2.5 (n/a)	Inside, close to Fe1 (6.12 Å)	Asp98 [$O^{\delta1}$; $O^{\delta2}$]	2.38; 3.62
					5× O [H_2O]	2.14; 2.28; 2.29; 2.54; 2.44
Fe3 (Mg)	1	57 (20)	11.2/4.5 (4.5/6.0)	Outer shell, 8.8 Å to 3-fold C-terminal axis	Asp132 [$O^{\delta1}$; $O^{\delta2}$]	2.51; 2.59
					Asp133 [$O^{\delta1}$; $O^{\delta2}$]	2.33; 3.56
					Asp 193 [$O^{\delta1}$; $O^{\delta2}$]	2.53; 4.25
					Asn195 [$O^{\delta1}$]	2.97
					Ile200 [O (carbonyl)]	2.19
					O [H_2O]	2.33
Fe4 (Fe)	1/3	69 (52)	5.5/3.7 (3.8/noise)	Internal, on the 3-fold N-terminal axis	Glu171 [$O^{\varepsilon1}$; $O^{\varepsilon2}$]	2.49; 4.57
					H_2O	3.32
Fe5 (n/a)	1	136	5.0/2.3 (n/a)	Internal, near to the 3-fold C-terminal axis	Asp87 [$O^{\delta1}$; $O^{\delta2}$]	2.51; 2.51

The values from the apo structure are between brackets. The numbering of the irons in the deposited pdb file 2C6R is from A1207–A1211. Note the assignment is classified following anomalous peak intensity.

[a] Peak height from anomalous maps above / below iron K absorption edge. The chelation mode or group from each residue is indicated in square brackets.

Lys67 at 2.74 Å distance and the position of residue Glu101 is stabilised by His174 at 3.47 Å and Lys178 at 3.76 Å. The displacements of residues observed between the apo-form and iron soaked models disrupts the salt-bridges between Lys67 and Asp97, Lys178 and Glu101 to the benefit of iron chelation. It is noteworthy that the amino acid residue Trp71 located in the neighbourhood of the ferroxidase centre, is well conserved amongst the members of the Dps family of proteins (Figure 3) although the function of this residue remains unclear. Residues His70, His82 and Trp78, situated close to Fe1, do not appear shifted significantly in the two structures.

A second iron site, Fe2, is located in the iron loaded structure at a distance of 6.1 Å from the ferroxidase iron site. The site is unusual in that most of the ligands of this ion are water molecules with only one direct (monodentate) ligand, Asp98, provided by the protein (Figure 2). Four water molecules (or hydroxyls) are distributed as a square in equatorial positions around Fe2 and another at 180 degrees from the Asp98 carbonyl moiety in the opposite apical position, resulting in an octahedral coordination of the iron. Two of these water molecules surrounding Fe2 are stabilised by hydrogen bonds to Lys94 and Lys178. Residues Asp98 and Lys94 form a salt-bridge in the apo-form structure with a separation of 2.69 Å. This salt-bridge appears weakened in the iron loaded structure with a shift of Lys94 away from Asp98 to a distance of 3.38 Å. Further structural displacements around site Fe2 were not observed comparing both the apo and iron loaded structure.

The channel created at the C-terminal 3-fold axis

The spherical assembly of the protein results in the formation of a total of eight 3-fold related channels out of which two distinct types of pores related by 3-fold symmetry are distinguished at each extremity of the four helix bundle. The four C-terminal pores per protein dodecamer are around 27 Å long and formed principally by residues Asp87, Glu83, Tyr79, Thr80, Leu77, Thr76, Asp199 and Phe198 (traversing the 3-fold axis from inside to the outside of the protein shell). Some of the residues with a polar side-chain such as Glu83, Tyr79 and Thr80 are found to be hydrated. The hydrophobic residues (i.e. Tyr79, Thr80, Leu77, Thr76) are located at the central region of this pore and protrude towards the 3-fold symmetry axis. The residues Asp199 and Phe198 are located in the external part of the 3-fold axis. The transit of cations along the channel appears to be blocked by residue Phe198 because of its hydrophobicity and the narrowing aperture (to 3.8 Å) formed between symmetry equivalents (Figure 4(a)). A transversal pathway formed by residues Thr76, Asp133, Asp199 and Ile200 is an alternative route for cations to the 3-fold axis for their exchange between the exterior and interior. This pathway leads to the exterior of the protein passing by a small cavity of roughly 5 to 6 Å diameter (being large enough to hold one or two cations) located at 8.8 Å from the 3-fold axis. Residues Asp132, Asp133, Asp193, Asn195 and Ile200 form principally the cavity (Ile200 chelating through its carbonyl group) with site Fe3 in the iron soaked crystal (Table 2) as shown by the phased anomalous difference maps.

Although the peak level for this site on the $|2F_o–F_c|$ map of the apo-form diffraction data is consistent with the presence of a water molecule, a peak was observed on the phased anomalous difference map from the same apo-form crystal, suggesting that a moeity other than water is bound in this position. However, considering the phased anomalous difference maps calculated from data

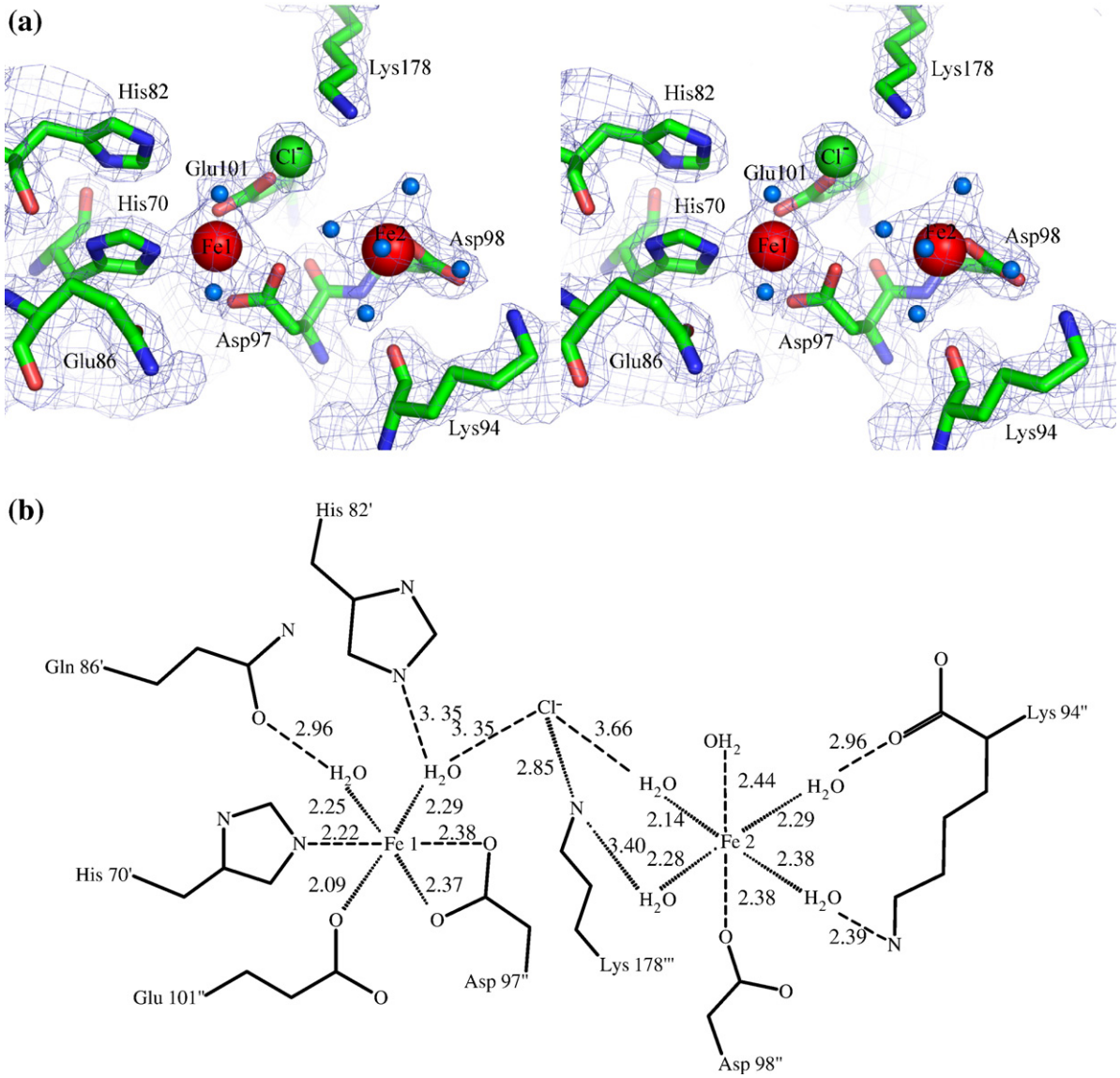

Figure 2. (a) Stereo representation of the electron densities at the ferroxidase centre at the dimer interface. The $|2F_o–F_c|$ map is coloured in blue and contoured at 2 σ. The ions are represented as spheres with iron coloured in red, chloride in green and the water molecules in light blue. Figure prepared with PyMOL [www.pymol.org]. (b) Schematic representation of the primary and secondary coordination sphere of the irons on the ferroxidase centre. Coordinating atoms are indicated by dotted lines and the distances are given in Å. Fe1 and Fe2 are separated by 6.1 Å. Figure prepared with ACD/ChemSketch 8.00 [www.acdlabs.com].

sets collected above and below iron edge (data not shown), the metal bound is not iron in the apo structure. It is likely that this site may be occupied by a magnesium ion as it is present in the crystallisation condition. The cavity site Fe3 is located at ca 10.6 Å from the exterior of the protein shell and the Fe3 sites related by 3-fold symmetry are separated by 15.2 Å. The iron site Fe5, only weakly chelated by residue Asp87, is found on the internal side of the 3-fold C-terminal pore. It exhibits the lowest anomalous signal amongst the iron sites and an extremely high *B*-factor of 136 Å^2 (ca four times the overall Wilson *B*-factor) at an occupancy of 1.0 in the refined structure. The anomalous signal for this site changes from above to below the iron K edge, confirming that it is most probably iron. Site Fe5 is close to the ferroxidase centre at distances of 9.8 Å and 12.3 Å to Fe1 and Fe2, respectively (Figure 1(a) and Table 2). Although site Fe5 may have been detected due to the high metal concentration used during the crystal soak, the proximity to the ferroxidase centre is suggestive of a role in iron transit between the C-terminal channel and the ferroxidase centre.

The channel created at the N-terminal 3-fold axis

The four 3-fold N-terminal interfaces, of approximately 17 Å length, are formed by the hydrophilic residues Glu171, Asn167, Gln170, Glu159 and Lys160 listed in order as the diameter of the funnel-shaped interface enlarges from 3.1 Å on its

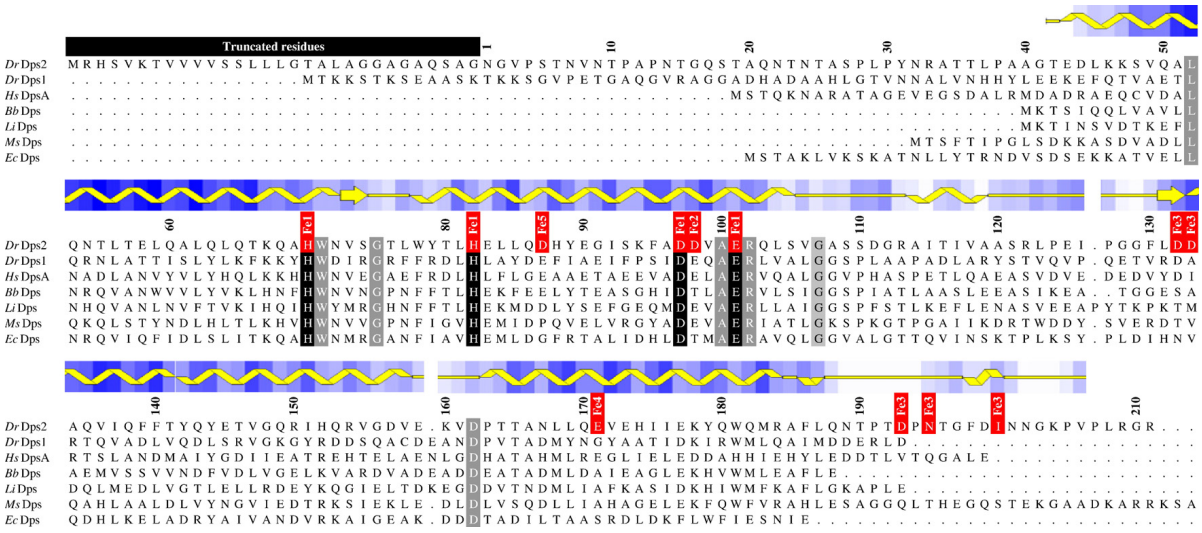

Figure 3. Sequence alignment of *Dr*Dps2 with key representatives of the Dps family. The bacterial Dps 1 and 2 from the radio-resistant *Dr* (*D. radiodurans*),[29,31] the Dps from *Bb* (*B. brevis*)[17] which harbours a labile di-nuclear ferroxidase centre and DNA-binding capability, *Li* (*L. innocua*)[4] Dps (or Flp) which does not bind DNA, *Ms* (*M. smegmatis*)[18] Dps which binds DNA with its C-terminal peptidic extension, *Ec* (*E. coli*)[59] Dps which binds DNA with the N-terminal peptidic extension and the archaeal *Hs* (*H. salinarum*)[6] Dps sharing the similar iron nucleation site to *Dr*Dps2. Numbering is for the cloned *Dr*Dps2. The secondary structure and the accessibility of the amino acid residues for *Dr*Dps2 given by PROCHECK[60] are shown above the alignment. The ligands for the ferroxidase centre are highlighted in black and the other iron sites are shown in red. Grey boxes represent completely conserved amino acid residues. The amino acid alignments were calculated using CLUSTALX.[35]

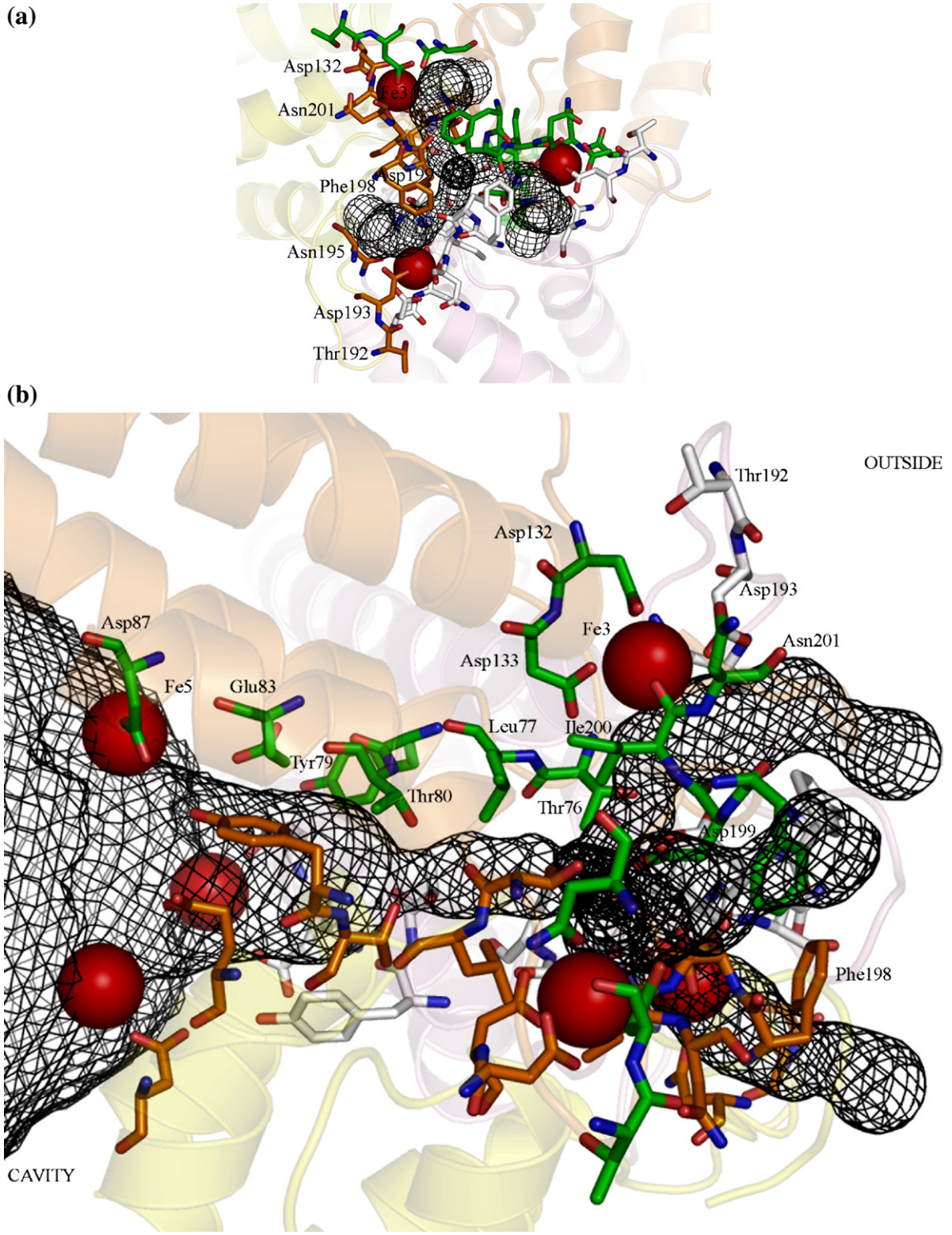

Figure 4. (a) Representation of the C-terminal channel seen along the 3-fold axis from outside the protein assembly. The symmetry-related Phe198 is closing the central 3-fold axis channel. (b) Profile view of the C-terminal channel complexity. The pathway available for cation transit is represented as a black isomesh calculated with the plug-in CAVER for PyMOL [www.pymol.org]. The residues present at the edge of the channel are contoured. The irons are represented as red spheres. Residues that belong to each distinct subunit are shown with a different colour. The local accessible diameters along the 3-fold C-terminal axis at the level of each residue are listed as follows: (from the cavity to the outer residue) Asp87 (12.2 Å), Glu83 (8.7 Å), Tyr79 (9.0 Å), Tr80 (3.2 Å), Leu77 (4.3 Å) and Thr76 (4.1 Å); (residues outside channel splitting) Asp199 (2.7 Å) and Phe198 (3.8 Å). The symmetry equivalent residues are not labelled on the Figures for better visibility.

internal side to 9.2 Å at the outer edge of the protein sphere. The three symmetry-related Glu171 form the ligands of the Fe4 binding site centred on the 3-fold axis (see Table 2). This iron site is located at a distance of 12.7 Å from Fe2 and 18.3 Å from Fe1 (the ferroxidase centre). Both the apo and iron soaked phased anomalous difference maps show a signal for iron in position Fe4 of similar magnitude. Lys160 from the external edge of the pore and Glu159 on the interior of the pore generate an electrostatic field potentially directing cations inside the protein shell.

Discussion

A high sequence homology of the 30 N-terminal residues with a signal anchor peptide was detected following problems in obtaining soluble full-length protein. The reason for a signal peptide on the *Dr*Dps2 protein remains unclear. This led us to express the truncated recombinant protein as described (Materials and Methods).

The toxicity of iron is mainly due to the reactivity of Fe(II) with oxygen leading to the formation of reactive oxygen species (superoxide, hydrogen peroxide, hydroxyl radicals). The occurrence of fast catalytic iron oxidation at the Dps ferroxidase centre and iron bio-entrapment is therefore of biological importance with respect to the inhibition of the formation of hydroxyl radicals,[42] which attack DNA sugars and bases, leading to degradation and strand breaks. The ferroxidase site organisation differs slightly between the known members of the Dps family of proteins although sequence alignment (Figure 3) shows that the residues involved in the binding of the mononuclear iron ferroxidase centres are conserved. Notably the sequence motifs of Asp97, Ala100, Glu101 and Arg102 (*Dr*Dps2 numbering) are conserved within Dps proteins harbouring ferroxidase activity.

The ferroxidase site Fe1 of *Dr*Dps2 and the ferroxidase centre of *Dr*Dps1[31] are octahedrally coordinated. In other Dps stuctures, tetrahedral (*B. anthracis*[10]) and pentahedral (*B. brevis*,[17] *A. tumefaciens*,[19] *M. smegmatis*[22]) coordination of the iron in the ferroxidase centre have been reported. The iron ferroxidase centre of *H. salinarum* DpsA in the reduced state was observed in a distorted hexagonal ligand coordination. The coordination geometries observed probably reflect different stages in iron biomineralisation. The ferroxidase centre of *Dr*Dps2 appears to present a di-nuclear-like iron binding site (Fe1 and Fe2) close to the dimer interface that differs structurally from the previously observed di-nuclear ferroxidase centres of ferritins with a typical inter-iron distance of 3.2 to 4.0 Å.[36,43–45] The primary and secondary coordination spheres of the ferroxidase centre observed in the iron soaked structure are shown in Figure 2.

The absence of a bridging ligand in the iron loaded structure of *Dr*Dps2 is observed at the ferroxidase centre iron sites Fe1 and Fe2. This is in contrast with the similar structure of the orthologue *B. brevis* Dps[17] observed with a di-nuclear ferroxidase centre. Indeed, *B. brevis* Dps[17] harbours a bridging carboxylate residue with a longer iron-carboxylate distance on site two than found in ferritin-like ferroxidase centres. The loosely coordinated site Fe2 of *Dr*Dps2 is chelated directly to the protein only through Asp98 with additional water-mediated contacts to His43 and Glu47, making this site more labile (reflected by higher *B*-factor obtained compared to Fe1: *B*-factor of 32 Å^2 for site Fe1 and 52 Å^2 for Fe2). Site Fe2 would be a metal transit site of the oxidation process taking place in the ferroxidase centre since it is compatible to bind either Fe(II) or Fe(III) according to the flexible, limited coordination and the respective change of the ionic radius with the charge of the iron.

Iron is present at site Fe3 in the iron soaked crystal, near to the 3-fold channel of the C-terminal. However, the situation is different for the apo-form crystal that has similar anomalous peak heights both above and below the iron K absorption edge for site Fe3 on both anomalous maps, suggesting the chelation of a metal other than iron is also possible on this site. Possible candidates for *in vivo* binding at this site would include calcium, which has strong involvement in biological regulation and has been thought to play a role in the uptake and release of iron as well as in iron biomineralisation from the Dps.[21,32] The interaction of calcium with *Dr*Dps1 has been reported to modify the kinetics of ferroxidation and favour the release of iron from a protein with mineralised iron core.[32] Grove *et al.* have suggested that the regulation for *Dr*Dps1 is induced by conformational changes generated by the binding of calcium to specific protein sites such as the ferroxidase centre and another unidentified site.[32] In the structure presented here, a metal site located in the channel away from, but close to, the C-terminal pore could act as a switch to this ion pathway.

The C-terminal channel can be thought of as an ion path with a valve system to control the flow of cations. The valve closure mechanism is formed by the 3-fold symmetry equivalent residues Phe198 and Asp199 at the outer edge of the C-terminal channel (Figure 4). In both the apo-form and iron soaked crystal structures the valve is closed, inhibiting cation transit. A second cation pathway is available nearby between residues Thr76, Asp133, Asp199 and Ile200 and directed away from the centre of the 3-fold axis but passing through the metallic site Fe3 (Figure 4(a) and (b)). Symmetry-related curved channels link the 3-fold C-terminal channel from below the 3-fold C-terminal axis valve residues (shown in Figures 4(a) and (b) and 5) to site Fe3 and to the surface of the protein. The charged residues surrounding Fe3 at the surface of the channel (Asp132, Asp 133, Asp193, Asn202, Lys204) facilitate cation entrance by creating an electrostatic potential directed towards site Fe3. Under iron uptake conditions, iron can be captured at site Fe3, migrate to the 3-fold axis and enter the protein central cage, bypassing the closed valve (see Figure 5). Nothing is

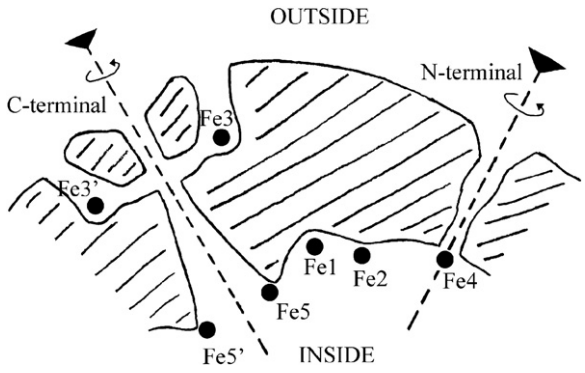

Figure 5. Schematic overview of the iron binding sites in *Dr*Dps2 showing their locations based on the iron soaked model. The dotted lines with top triangles show the 3-fold axis (C-terminal on the left and N-terminal on the right). The relative distances are respected between the irons. The protein is symbolised by the cross-hatched surface.

yet known concerning the structural layout of the residues 190–211 in the absence of a metal bound on site Fe3. However, it is not unreasonable to assume that these residues may be able to change conformation and reorganise due to their higher flexibility in the structure, making the C-terminal channel compatible with both iron entrance and release from the protein. *Dr*Dps1[31,39] and *L. lactis* Dps[36] harbour a metallic coordination site at the outer surface of the protein shell at the N-terminal side of the protein whereas the equivalent metal binding site is found at the C-terminal part in *Dr*Dps2.

The crystal of *Dr*Dps2 soaked in iron solution presents a similar nucleation site to that previously observed near to Glu154 of the orthologue *H. salinarum (Hs)* DpsA[6] (equivalent to Glu171 in the *D. radiodurans* Dps2; shown in Figure 3) with a single iron position, Fe4, held between the three symmetry-related Glu171 residues. An inorganic assembly of the intermediate iron biomineralisation stage, forming a [4Fe-3O] half prism shaped cluster, has been observed in *Hs*DpsA[6]. In the structure presented here, the neighbourhood of the site Fe4 exhibits a low electron density in the phased anomalous difference maps, possibly representing an earlier disordered nucleation stage of biomineralisation compared to the *Hs*DpsA[6] stucture.

A structure-based sequence alignment indicated the equivalence of the iron site chelated by Glu171 (ligand for site Fe4) from *Dr*Dps2 with the nucleation site bound by Glu154 in *Hs*DpsA (not shown). The structure of *Hs*DpsA[6] has an N-terminal interface aperture smaller by around 1 Å than the corresponding interface of *Dr*Dps2. In *Hs*Dps, the structurally equivalent channel has been reported to be closed and to have an iron nucleation centre bound to Glu154[6]. The positively charged residue Lys160 is present on the edge of the N-terminal channel with the acidic residue Glu159 inside the pore creating an electrostatic field directed towards inside the cage and suggesting that cations would be attracted through the channel, as has been suggested for the 3-fold symmetry axis present in the sphere-forming ferritin families,[45,46] making this a possible Fe(II) entrance pathway.[17,20] However, the site formed by the Glu171 residues should be free of a growing oxidised nucleus in order that fresh Fe(II) may enter through the channel.

Iron incorporation in Dps could occur in distinct steps involving the capture and migration of Fe(II) to the ferroxidase centre, Fe(II) oxidation, Fe(III) migration for the nucleation and growth of a mineral core as already reported for ferritins.[14] Iron transit through the C-terminal channel is suggested by the presence, in the iron soaked crystal, of site Fe3 at the external side of the channel and Fe5 at the interior end of the channel 9.8 Å away from the ferroxidase centre. Fast catalytic iron oxidation with the appropriate oxidant would occur after iron binding to the high affinity ferroxidase centre. Oxidised iron would then bind to residue Asp98 (the site Fe2 ligand) to be displaced to the 12.8 Å distant nucleation site Fe4 mediated by the polar residue His174 present in a pocket along the Fe2 to Fe4 path.

Although it is more likely that the efficient DNA repair system in *D. radiodurans* represents an adaptation to prolonged desiccation, it has developed mechanisms to minimise the consequences of DNA double-strand breaks generated by ionising radiation.[47] This can be achieved by passively preventing break formation, by repairing the breaks and preventing the loss of information and by having as many as ten genome copies per cell.[48,49] The anti-oxidative protective role of *Dr*Dps2 may extend to non-specific DNA binding and enhance DNA sheltering making it less sensitive to degradation. It has been demonstrated before that DNA binding cannot be predicted reliably on the basis of the sequence of the peptidic extremities.[19] Indeed, the disordered 41 residue N-terminal extension of *Dr*Dps2 is poor in arginine residues (only one) and does not possess any lysine residues, both of which usually play a role in DNA binding by electrostatic interactions with negatively charged DNA. However, the short C-terminus of the protein contains one lysine and two arginine residues. Protection could also be mediated by hooking of the DNA double strand by the mobile N-terminal extension protruding from the Dps sphere.

The combination of non-specific DNA binding properties with iron entrapment and detoxification is a strong beneficial combination of properties that Dps gathers for the protection of cells and the determination of the *Dr*Dps2 structure is a first step in the understanding of its probable involvement in the radiation resistance of *D. radiodurans*. Further work will be required to confirm the implications of metal binding on specific sites like Fe3 close to the C-terminal channel, as well as establishing the mechanistic details of iron uptake by *Dr*Dps2.

Materials and Methods

Protein production and purification

Attempts to obtain a soluble construct of the full-length DRB0092 (*Dr*Dps2) protein failed. DRB0092 was cloned using the Gateway system pDest14 (Invitrogen) with a construct that suppressed the codons for the 30 first amino acid residues. The protein referred to here is the cloned protein from residues 31 to 241, but the residue numbering as annotated in the TIGR database† is shifted by 30 removed residues in the deposited structures described. The truncated *Dr*Dps2 was expressed in *E. coli* DE3 cells with 100 μg/ml ampicillin in LB media. Induction with 1 mM IPTG was done at an $A_{600\ nm}$ of 0.6 and the *E. coli* cells were grown overnight at 20 °C. The *E. coli* cells were collected by centrifugation at 7000*g* for 10 min and resuspended in 10 ml of 50 mM Tris-HCl (pH 7.2). The *E. coli* cells were broken using a French press (9000 psi) in the presence of DNase I and protease inhibitors. The supernatant was collected after centrifugation at 20,000*g* for 40 min. The soluble extract was heated twice at 70 °C for 30 min (to denature and separate other less stable proteins present in the mixture) and centrifuged for 10 min at 7000*g* after each step. The supernatant was then loaded on an anionic exchange chromatography column (HP-Q, 5 ml) previously equilibrated with 50 mM Tris-HCl (pH 7.2) at room temperature. The main *Dr*Dps2 fraction was eluted at 300 mM NaCl. These fractions were concentrated and loaded on to a gel filtration chromatography column (Superdex 200–XK 16/60). Pure *Dr*Dps2 was eluted in the fractions between 65 to 80 ml of retention volumes using 50 mM Tris-HCl (pH 7.2), 150 mM NaCl buffer, and sample purity checked with SDS-PAGE analysis.

Crystallisation

Crystallisation conditions were screened using concentrated protein solution (11 mg/ml) and the Hampton Natrix crystal screen‡ with the hanging-drop vapour diffusion technique at 20 °C in multi well plates. Each well was filled with 100 μl of reservoir solution. Cubic crystals were obtained after a period of equilibration of four weeks. Crystals suitable for X-ray diffraction experiments were obtained from 2 μl drops consisting of a 1:1 mixture of *Dr*Dps2 protein (50 mM Tris-HCl (pH 7.2), 150 mM NaCl) and 10 mM magnesium chloride, 50 mM Tris-HCl (pH 7.5), 5% (v/v) isopropanol (Hampton Natrix crystal screen number 42) placed on cover slips and left for equilibration against the reservoir solution. The typical cubic crystal size obtained was of 25 μm × 25 μm × 25 μm.

X-ray data collection processing and refinement

X-ray data were collected either at ESRF beamline ID14-2[50] or ID23-1[51] on a total of three cryo-cooled crystals. Cryo-protection was obtained by passing crystals rapidly through a solution of 25% (v/v) glycerol in the mother liquor. A dataset to 2.05 Å resolution was collected from a cryo-cooled apo-form crystal (crystal A) using X-rays of wavelength of 0.933 Å on beamline ID14-2. A crystal (crystal B) soaked in 0.1 M $(NH_4)_2Fe(SO_4)_2$ solution for 20 min was exposed to attenuated beam to obtain redundant anomalous differences to 2.8 Å resolution on beamline ID23-1 for phasing purpose. Data images were integrated with MOSFLM,[52] scaled using the CCP4 software SCALA[29,53] and converted to structure factors with TRUNCATE.[53] The data were used as input to autoSHARP[54] for single wavelength anomalous diffraction (SAD) phasing, which detected five irons and one sulphur per asymmetric unit. The statistics for phasing are shown in Table 1.

To locate the iron binding sites still missing in the apo structure of *Dr*Dps2, another cryo-cooled iron soaked crystal (crystal C, using the same conditions as above) was used to obtain three data sets to higher resolution (at a wavelength of 1.1070 Å) and just above (1.7377 Å) and just below (1.7451 Å) the iron K absorption edge to resolutions of 2.1 Å, 2.3 Å and 2.3 Å, respectively. The data treatment was as detailed above. Phases calculated from both final models were applied to the various data sets in order to generate phased anomalous difference maps and therefore confirm the locations and identity of iron atoms in the structure. The datasets collected above and below the iron edge on crystal C have negligible *B*-factor differences suggesting that radiation damage was not a significant issue.

For both the apo (crystal A) and the iron soaked crystal (crystal C, high energy 1.1070 Å data), phase information obtained from the highly redundant iron soaked crystal was merged with the structure factor data (CAD). Automatic construction using arp/WARP[53,55] resulted in models of 156 and 149 residues, respectively, for the apo and iron soaked models. Cycles of manual reconstruction using COOT[56] and refinement with automatic water placement using REFMAC and arp/WARP[29,53,57] were used to complete the model. For the final step of the refinements, all available reflections were included (Table 1).

Protein Data Bank accession codes

The refined structures have been deposited with the RCSB Protein Data Bank and are available under accession codes 2C2J for the apo and 2C6R for the iron soaked crystal structures.

† www.tigr.org
‡ www.hamptonresearch.com

Acknowledgement

This work is supported by the European Synchrotron Radiation Facility (ESRF, Grenoble, France).

References

1. Wiedenheft, B., Mosolf, J., Willits, D., Yeager, M., Dryden, K. A., Young, M. & Douglas, T. (2005). An archaeal antioxidant: characterization of a Dps-like protein from *Sulfolobus solfataricus*. *Proc. Natl Acad. Sci. USA*, **102**, 10551–10556.
2. Ceci, P., Ilari, A., Falvo, E., Giangiacomo, L. & Chiancone, E. (2005). Reassessment of protein stability, DNA binding, and protection of *Mycobacterium smegmatis* Dps. *J. Biol. Chem.* **280**, 34776–34785.
3. Ramsay, B., Wiedenheft, B., Allen, M., Gauss, G. H., Lawrence, C. M., Young, M. & Douglas, T. (2006). Dps-like protein from the hyperthermophilic archaeon *Pyrococcus furiosus*. *J. Inorg. Biochem.* **100**, 1061–1068.

4. Su, M., Cavallo, S., Stefanini, S., Chiancone, E. & Chasteen, N. D. (2005). The so-called *Listeria innocua* ferritin is a Dps protein. Iron incorporation, detoxification, and DNA protection properties. *Biochemistry*, **44**, 5572–5578.
5. Johnson, E., Cascio, D., Sawaya, M. R., Gingery, M. & Schroder, I. (2005). Crystal structures of a tetrahedral open pore ferritin from the hyperthermophilic archaeon *Archaeoglobus fulgidus*. *Structure (Camb.)*, **13**, 637–648.
6. Zeth, K., Offermann, S., Essen, L. O. & Oesterhelt, D. (2004). Iron-oxo clusters biomineralizing on protein surfaces: structural analysis of *Halobacterium salinarum* DpsA in its low- and high-iron states. *Proc. Natl Acad. Sci. USA*, **101**, 13780–13785.
7. Nicodeme, M., Perrin, C., Hols, P., Bracquart, P. & Gaillard, J. L. (2004). Identification of an iron-binding protein of the Dps family expressed by *Streptococcus thermophilus*. *Curr. Microbiol.* **48**, 51–56.
8. Halsey, T. A., Vazquez-Torres, A., Gravdahl, D. J., Fang, F. C. & Libby, S. J. (2004). The ferritin-like Dps protein is required for *Salmonella enterica* serovar typhimurium oxidative stress resistance and virulence. *Infect. Immun.* **72**, 1155–1158.
9. Roy, S., Gupta, S., Das, S., Sekar, K., Chatterji, D. & Vijayan, M. (2003). Crystallization and preliminary X-ray diffraction analysis of *Mycobacterium smegmatis* Dps. *Acta Crystallog. sect. D*, **59**, 2254–2256.
10. Papinutto, E., Dundon, W. G., Pitulis, N., Battistutta, R., Montecucco, C. & Zanotti, G. (2002). Structure of two iron-binding proteins from *Bacillus anthracis*. *J. Biol. Chem.* **277**, 15093–15098.
11. Haataja, S., Penttinen, A., Pulliainen, A. T., Tikkanen, K., Finne, J. & Papageorgiou, A. C. (2002). Expression, purification and crystallization of Dpr, a ferritin-like protein from the Gram-positive meningitis-associated bacterium *Streptococcus suis*. *Acta Crystallog. sect. D*, **58**, 1851–1853.
12. Grant, R. A., Filman, D. J., Finkel, S. E., Kolter, R. & Hogle, J. M. (1998). The crystal structure of Dps, a ferritin homolog that binds and protects DNA. *Nature Struct. Biol.* **5**, 294–303.
13. Chen, L. & Helmann, J. D. (1995). *Bacillus subtilis* MrgA is a Dps(PexB) homologue: evidence for metalloregulation of an oxidative-stress gene. *Mol. Microbiol.* **18**, 295–300.
14. Harrison, P. M. & Arosio, P. (1996). Ferritins: molecular properties, iron storage function and cellular regulation. *Biochim. Biophys. ActaBioenerget.* **1275**, 161–203.
15. Chasteen, N. D. (1998). Ferritin. Uptake, storage, and release of iron. *Met. Ions Biol. Syst.* **35**, 479–514.
16. Theil, E. C. (2003). Ferritin: at the crossroads of iron and oxygen metabolism. *J. Nutrition*, **133**, 1549s–1553s.
17. Ren, B., Tibbelin, G., Kajino, T., Asami, O. & Ladenstein, R. (2003). The multi-layered structure of Dps with a novel di-nuclear ferroxidase center. *J. Mol. Biol.* **329**, 467–477.
18. Gupta, S. & Chatterji, D. (2003). Bimodal protection of DNA by *Mycobacterium smegmatis* DNA-binding protein from stationary phase cells. *J. Biol. Chem.* **278**, 5235–5241.
19. Ceci, P., Ilari, A., Falvo, E. & Chiancone, E. (2003). The Dps protein of *Agrobacterium tumefaciens* does not bind to DNA but protects it toward oxidative cleavage: X-ray crystal structure, iron binding, and hydroxyl-radical scavenging properties. *J. Biol. Chem.* **278**, 20319–20326.
20. Ilari, A., Stefanini, S., Chiancone, E. & Tsernoglou, D. (2000). The dodecameric ferritin from *Listeria innocua* contains a novel intersubunit iron-binding site. *Nature Struct. Biol.* **7**, 38–43.
21. Kauko, A., Haataja, S., Pulliainen, A. T., Finne, J. & Papageorgiou, A. C. (2004). Crystal structure of *Streptococcus suis* Dps-like peroxide resistance protein Dpr: implications for iron incorporation. *J. Mol. Biol.* **338**, 547–558.
22. Roy, S., Gupta, S., Das, S., Sekar, K., Chatterji, D. & Vijayan, M. (2004). X-ray analysis of *Mycobacterium smegmatis* Dps and a comparative study involving other Dps and Dps-like molecules. *J. Mol. Biol.* **339**, 1103–1113.
23. Zhao, G., Ceci, P., Ilari, A., Giangiacomo, L., Laue, T. M., Chiancone, E. & Chasteen, N. D. (2002). Iron and hydrogen peroxide detoxification properties of DNA-binding protein from starved cells. A ferritin-like DNA-binding protein of *Escherichia coli*. *J. Biol. Chem.* **277**, 27689–27696.
24. Yamamoto, Y., Poole, L. B., Hantgan, R. R. & Kamio, Y. (2002). An iron-binding protein, Dpr, from *Streptococcus mutans* prevents iron-dependent hydroxyl radical formation *in vitro*. *J. Bacteriol.* **184**, 2931–2939.
25. Ilari, A., Ceci, P., Ferrari, D., Rossi, G. L. & Chiancone, E. (2002). Iron incorporation into *Escherichia coli* Dps gives rise to a ferritin-like microcrystalline core. *J. Biol. Chem.* **277**, 37619–37623.
26. Nair, S. & Finkel, S. E. (2004). Dps protects cells against multiple stresses during stationary phase. *J. Bacteriol.* **186**, 4192–4198.
27. Wardman, P. & Candeias, L. P. (1996). Fenton chemistry: an introduction. *Radiat. Res.* **145**, 523–531.
28. Krasin, F. & Hutchinson, F. (1981). Repair of DNA double-strand breaks in *Escherichia coli* cells requires synthesis of proteins that can be induced by UV light. *Proc. Natl Acad. Sci. USA*, **78**, 3450–3453.
29. White, O., Eisen, J. A., Heidelberg, J. F., Hickey, E. K., Peterson, J. D., Dodson, R. J. *et al.* (1999). Genome sequence of the radioresistant bacterium *Deinococcus radiodurans* R1. *Science*, **286**, 1571–1577.
30. Battista, J. R. (1997). Against all odds: the survival strategies of *Deinococcus radiodurans*. *Annu. Rev. Microbiol.* **51**, 203–224.
31. Romao, C. V., Mitchell, E. P. & McSweeney, S. (2006). The crystal structure of *Deinococcus radiodurans* Dps protein (DR2263) reveals the presence of a novel metal centre in the N terminus. *J. Biol. Inorg. Chem.* **11**, 891–902.
32. Grove, A. & Wilkinson, S. P. (2005). Differential DNA binding and protection by dimeric and dodecameric forms of the ferritin homolog Dps from *Deinococcus radiodurans*. *J. Mol. Biol.* **347**, 495–508.
33. Theil, E. C., Matzapetakis, M. & Liu, X. (2006). Ferritins: iron/oxygen biominerals in protein nanocages. *J. Biol. Inorg. Chem.* **11**, 803–810.
34. Liu, X., Kim, K., Leighton, T. & Theil, E. C. (2006). Paired *Bacillus anthracis* Dps (mini-ferritin) have different reactivities with peroxide. *J. Biol. Chem.* **281**, 27827–27835.
35. Liu, Y., Zhou, J., Omelchenko, M. V., Beliaev, A. S., Venkateswaran, A., Stair, J. *et al.* (2003). Transcriptome dynamics of *Deinococcus radiodurans* recovering from ionizing radiation. *Proc. Natl Acad. Sci. USA*, **100**, 4191–4196.
36. Stillman, T. J., Upadhyay, M., Norte, V. A., Sedelnikova, S. E., Carradus, M., Tzokov, S. *et al.* (2005). The crystal structures of *Lactococcus lactis* MG1363 Dps proteins reveal the presence of an N-terminal helix that is required for DNA binding. *Mol. Microbiol.* **57**, 1101–1112.

37. Bozzi, M., Mignogna, G., Stefanini, S., Barra, D., Longhi, C., Valenti, P. & Chiancone, E. (1997). A novel non-heme iron-binding ferritin related to the DNA-binding proteins of the Dps family in *Listeria innocua*. *J. Biol. Chem.* **272**, 3259–3265.
38. Zanotti, G., Papinutto, E., Dundon, W., Battistutta, R., Seveso, M., Giudice, G. *et al.* (2002). Structure of the neutrophil-activating protein from *Helicobacter pylori*. *J. Mol. Biol.* **323**, 125–130.
39. Kim, S. G., Bhattacharyya, G., Grove, A. & Lee, Y. H. (2006). Crystal structure of Dps-1, a functionally distinct Dps protein from *Deinococcus radiodurans*. *J. Mol. Biol.* **361**, 105–114.
40. Ramachandran, G. N., Ramakrishnan, C. & Sasisekharan, V. (1963). Stereochemistry of polypeptide chain configurations. *J. Mol. Biol.* **7**, 95–99.
41. Kleywegt, G. J. & Jones, T. A. (1994). Detection, delineation, measurement and display of cavities in macromolecular structures. *Acta Crystallog. sect. D*, **50**, 178–185.
42. Halliwell, B. & Gutteridge, J. M. (1984). Oxygen toxicity, oxygen radicals, transition metals and disease. *Biochem. J.* **219**, 1–14.
43. Macedo, S., Romao, C. V., Mitchell, E., Matias, P. M., Liu, M. Y., Xavier, A. V. *et al.* (2003). The nature of the di-iron site in the bacterioferritin from *Desulfovibrio desulfuricans*. *Nature Struct. Biol.* **10**, 285–290.
44. Hempstead, P. D., Hudson, A. J., Artymiuk, P. J., Andrews, S. C., Banfield, M. J., Guest, J. R. & Harrison, P. M. (1994). Direct observation of the iron binding sites in a ferritin. *FEBS Letters*, **350**, 258–262.
45. Chasteen, N. D. & Harrison, P. M. (1999). Mineralization in ferritin: an efficient means of iron storage. *J. Struct. Biol.* **126**, 182–194.
46. Douglas, T. & Ripoll, D. R. (1998). Calculated electrostatic gradients in recombinant human H-chain ferritin. *Protein Sci.* **7**, 1083–1091.
47. Mattimore, V. & Battista, J. R. (1996). Radioresistance of *Deinococcus radiodurans*: functions necessary to survive ionizing radiation are also necessary to survive prolonged desiccation. *J. Bacteriol.* **178**, 633–637.
48. Battista, J. R. (2000). Radiation resistance: the fragments that remain. *Curr. Biol.* **10**, R204–R205.
49. Dean, C. J., Ormerod, M. G., Serianni, R. W. & Alexander, P. (1969). DNA strand breakage in cells irradiated with X-rays. *Nature*, **222**, 1042–1044.
50. Wakatsuki, S., Belrhali, H., Mitchell, E. P., Burmeister, W. P., McSweeney, S. M., Kahn, R. *et al.* (1998). ID14 'Quadriga', a beamline for protein crystallography at the ESRF. *J. Synchrotron Radiat.* **5**, 215–221.
51. Biasci, J. C., Plan, B. & Zhang, L. (2002). Design and performance of ESRF high-power undulator front-end components. *J. Synchrotron Radiat.* **9**, 44–46.
52. Powell, H. R. (1999). The Rossmann Fourier autoindexing algorithm in MOSFLM. *Acta Crystallog. sect. D*, **55**, 1690–1695.
53. Collaborative Computational Project, Nunber 4 (1994). The CCP4 suite: programs for protein crystallography. *Acta Crystallog. sect. D*, **50**, 760–763.
54. Bricogne, G., Vonrhein, C., Flensburg, C., Schiltz, M. & Paciorek, W. (2003). Generation, representation and flow of phase information in structure determination: recent developments in and around SHARP 2.0. *Acta Crystallog. sect. D*, **59**, 2023–2030.
55. Perrakis, A., Morris, R. & Lamzin, V. S. (1999). Automated protein model building combined with iterative structure refinement. *Nature Struct. Biol.* **6**, 458–463.
56. Emsley, P. & Cowtan, K. (2004). Coot: model-building tools for molecular graphics. *Acta Crystallog. sect. D*, **60**, 2126–2132.
57. Murshudov, G. N., Vagin, A. A. & Dodson, E. J. (1997). Refinement of macromolecular structures by the maximum-likelihood method. *Acta Crystallog. sect. D*, **53**, 240–255.
58. Weiss, M. S. (2001). Global indicators of X-ray data quality. *J. Appl. Crystall.* **34**, 130–135.
59. Ceci, P., Cellai, S., Falvo, E., Rivetti, C., Rossi, G. L. & Chiancone, E. (2004). DNA condensation and self-aggregation of *Escherichia coli* Dps are coupled phenomena related to the properties of the N-terminus. *Nucl. Acids Res.* **32**, 5935–5944.
60. Laskowski, R., MacArthur, M., Moss, D. & Thornton, J. (1993). PROCHECK - program to check the stereochemical quality of proteins. *J. Appl. Crystallog.* **26**, 283–291.

Edited by R. Huber

(Received 2 August 2006; received in revised form 6 November 2006; accepted 8 November 2006)
Available online 11 November 2006